# Stacking X-ray Observations of "Little Red Dots": Implications for their AGN Properties

Minghao Yue ,[1] Anna-Christina Eilers ,[1] Tonima Tasnim Ananna ,[2] Christos Panagiotou,[1] Erin Kara ,[1]
and Takamitsu Miyaji [3]

[1]MIT Kavli Institute for Astrophysics and Space Research, 77 Massachusetts Ave., Cambridge, MA 02139, USA
[2]Department of Physics and Astronomy, Wayne State University, 666 W Hancock St, Detroit, MI 48201, USA
[3]Instituto de Astronomía, Universidad Nacional Autónoma de México Campus Ensenada, A.P. 106, Ensenada, BC 22800, Mexico

## ABSTRACT

Recent *James Webb Space Telescope (JWST)* observations have revealed a population of compact extragalactic objects at $z \gtrsim 4$ with red near-infrared colors, which have been dubbed as "Little Red Dots" (LRDs). The spectroscopically-selected LRDs exhibit broad H$\alpha$ emission lines, which has led to the conclusion that type-I active galactic nuclei (AGN) are harbored in the galaxies' dust-reddened cores. However, other mechanisms, like strong outflowing winds, could also produce broad H$\alpha$ emission lines, and thus, the nature of LRDs is still under debate. In this work, we test the AGN hypothesis for LRDs by stacking the archival *Chandra* observations of 19 spectroscopically-selected LRDs. We obtain non-detections in both the soft $(0.5 - 2 \text{ keV})$ and the hard $(2 - 8 \text{ keV})$ X-ray band after stacking, and put upper limits on the X-ray luminosities of these LRDs. We find that the soft band upper limit is $\sim 1$ dex lower than the expected level from the $L_{\text{X}} - L_{\text{H}\alpha}$ relation, while the hard band upper limit is consistent with this relation. This result suggests that LRDs and typical type-I AGNs have significantly different properties. We consider it unlikely that absorption is the main reason for the observed low $L_{\text{X}}/L_{\text{H}\alpha}$ ratios of LRDs. Alternatively, we discuss two plausible hypotheses: (1) LRDs have intrinsically weak X-ray emissions, (2) fast, galactic-scale outflows have a major contribution to the observed broad H$\alpha$ lines. Our findings indicate that empirical relations (e.g., for black hole mass measurements) established for typical type-I AGNs should be used with caution when analyzing the properties of LRDs.

*Keywords:* Active Galactic Nuclei

## 1. INTRODUCTION

The recent launch of the *James Webb Space Telescope* (JWST) has opened new windows towards studies of distant galaxies and supermassive black holes (SMBHs). One particularly exciting discovery by *JWST* is the abundant population of so-called "little red dots" (LRDs). LRDs are compact objects at $z \gtrsim 4$ with very red near-infrared color, which have been found by many *JWST* survey programs (e.g., Labbe et al. 2023; Kocevski et al. 2023; Harikane et al. 2023; Matthee et al. 2023; Greene et al. 2023). Their spectra exhibit broad H$\alpha$ emission lines, suggesting type-I active galactic nuclei (AGN) activity in their cores. The number density

Corresponding author: Minghao Yue
myue@mit.edu

of LRDs at $z \sim 5$ is about $10^{-5} - 10^{-4} \text{ Mpc}^{-3}\text{mag}^{-1}$ (e.g., Greene et al. 2023), which is $\sim 1 - 2$ dex higher than the faint end of quasar luminosity functions (e.g., Matsuoka et al. 2018; Schindler et al. 2023). This comparison suggests that LRDs might be a population of previously unexplored dust-reddened AGNs, and that our current picture of SMBH-galaxy co-evolution might be incomplete.

However, the properties of LRDs are still largely unclear, and a few models have been proposed to explain the observed features of these objects. Kocevski et al. (2023) found that the spectral energy distributions (SEDs) of LRDs can be explained either by a dust-obscured AGN plus a blue galaxy or by an unobscured AGN combined with a red galaxy. Labbe et al. (2023) and Greene et al. (2023) suggested that LRDs might be heavily obscured AGNs and that the broad emission lines and rest-frame UV continuum of LRDs might arise

from the scattered light of the central AGNs. Matthee et al. (2023) proposed that LRDs represent a transition phase from heavily obscured AGNs to unobscured quasars. This model is in line with Noboriguchi et al. (2023), who found that LRDs share similar features with blue-excess dust-obscured galaxies (BluDOGs) at lower redshifts.

Nevertheless, type-I AGNs are not the only plausible scenario that can explain the observational features of LRDs. Strong outflows in compact regions, likely driven by supernovae or star formation, can also generate broad H$\alpha$ emission lines. This possibility has been discussed in, e.g., Matthee et al. (2023). This uncertainty prevents us from further understanding the properties of LRDs and their implications on galaxy evolution models. Confirming the nature of LRDs requires multi-wavelength observations that can unambiguously reveal signs of AGN activity. Some efforts have been carried out using the Mid-Infrared Instrument (MIRI) on JWST, aiming at detecting the hot dust emission heated by the AGN. For example, Pérez-González et al. (2024) analyzed the NIRCam and MIRI observations of 31 photometrically-selected LRDs and performed SED fitting to test the AGN hypothesis. The authors found that the mid-infrared emissions of the LRDs are inconsistent with an AGN dust torus, potentially indicating that the SEDs of LRDs might not be AGN-dominated.

X-ray emission is one of the most reliable indicators of AGN activity. Several studies have investigated the X-ray emission of LRDs in the Chandra deep fields (e.g., Matthee et al. 2023; Lyu et al. 2023), who reported non-detections for all the LRDs in their sample. Wang et al. (2024) reported a luminous LRD at $z = 3.1$ with an X-ray flux upper limit that is $\sim 100$ times weaker than the expectation from its optical luminosity. Inayoshi & Ichikawa (2024) indicate that current X-ray observations are not deep enough to detect the X-ray emission for most individual LRDs. Meanwhile, Kocevski et al. (2024) recently discovered two bright photometrically-selected LRDs detected in Chandra deep fields, which have $L_{\rm X}(2 - 10 \text{ keV}) \sim 10^{44}$ erg s$^{-1}$ and $N_{\rm H} \sim 10^{23} \text{cm}^{-2}$. The diverse results demonstrate that our knowledge about the X-ray properties of LRDs are still highly limited.

Since most LRDs do not have X-ray detections, a stacking analysis offers a viable way to investigate the X-ray properties of these objects. In this letter, we aim to detect or put more stringent constraints on the X-ray fluxes of LRDs by stacking archival Chandra observations. We describe our sample and the stacking procedure in Section 2. The results are presented in Section 3. We discuss the implication of our results in Section 4 and conclude in Section 5. We adopt a flat $\Lambda$CDM cosmology with $H_0 = 70$ km s$^{-1}$ Mpc$^{-1}$ and $\Omega_M = 0.3$.

## 2. STACKING THE CHANDRA OBSERVATIONS OF LITTLE RED DOTS

### 2.1. Sample Selection

We construct the sample for this work by compiling known spectroscopically-selected LRDs from the literature. We notice that the LRD samples in many studies are defined purely based on NIRCam photometry and do not have spectroscopic confirmation. Since we focus on testing the type-I AGN hypothesis, in this work, we focus on objects with broad H$\alpha$ emission lines (FWHM$_{\rm H\alpha} > 1000$ km s$^{-1}$) confirmed by spectroscopy.

The parent sample consists of objects from Harikane et al. (2023), Matthee et al. (2023), and Maiolino et al. (2023) that have archival Chandra ACIS-I observations. [1] We do not include objects that are covered by other Chandra instruments and other X-ray telescopes, as the stacking software we use, CSTACK (Miyaji et al. 2008), is currently only implemented to work on ACIS-I observations. We also exclude objects found in lensing cluster fields (e.g., those in Greene et al. 2023), which could suffer contamination from the X-ray emission of the foreground galaxy cluster. During the stacking process (Section 2.2), we further exclude objects with close companions or uneven background by visual inspection, for which the background subtraction might be inaccurate.

The final sample consists of 19 LRDs summarized in Table 1. These LRDs are at $4 < z < 7$ and are located in several Chandra deep fields, including AEGIS (Laird et al. 2009), CDF-N (Brandt et al. 2001), and CDF-S (Rosati et al. 2002). The typical exposure time for these objects is $\sim 10^6$ seconds.

### 2.2. Stacking Analysis

We use CSTACK (Miyaji et al. 2008)[2] to stack the archival Chandra observations. CSTACK is an online stacking tool that analyzes archival ACIS-I observations in several Chandra deep fields. To compute the stacked flux for a sample of objects, CSTACK takes the positions of objects as inputs and sums the photons within certain apertures at these positions. In this work, we only in-

---

[1] We note that Kocevski et al. (2024) recently reported 17 new spectroscopically-confirmed LRDs. However, we do not include these objects as their H$\alpha$ luminosities were not available, which is a key part in our analysis (see Section 3).

[2] http://lambic.astrosen.unam.mx/cstack/

**Table 1.** The LRD sample for stacking

| Name | RA | Dec | Redshift | $\log L_{\mathrm{H}\alpha}$ | $\mathrm{FWHM}_{\mathrm{H}\alpha}$ | $\log M_{\mathrm{BH}}$[1] | Reference |
|---|---|---|---|---|---|---|---|
| | (deg) | (deg) | | (erg s$^{-1}$) | km s$^{-1}$ | ($M_\odot$) | |
| CEERS-00397 | 214.83621 | 52.88269 | 6.000 | $42.41^{+0.12}_{-0.07}$ | $1739^{+359}_{-317}$ | $7.00^{+0.26}_{-0.30}$ | Harikane et al. (2023) |
| CEERS-00672 | 214.88967 | 52.83297 | 5.666 | $43.26^{+0.05}_{-0.05}$ | $2208^{+277}_{-241}$ | $7.70^{+0.13}_{-0.13}$ | Harikane et al. (2023) |
| CEERS-00717 | 215.08142 | 52.97219 | 6.936 | $42.08^{+0.10}_{-0.08}$ | $6279^{+805}_{-881}$ | $7.99^{+0.16}_{-0.17}$ | Harikane et al. (2023) |
| CEERS-00746 | 214.80912 | 52.86847 | 5.624 | $43.83^{+0.02}_{-0.03}$ | $1660^{+157}_{-162}$ | $7.76^{+0.10}_{-0.11}$ | Harikane et al. (2023) |
| CEERS-01236 | 215.14529 | 52.96728 | 4.484 | $41.68^{+0.09}_{-0.08}$ | $3521^{+649}_{-485}$ | $7.26^{+0.19}_{-0.18}$ | Harikane et al. (2023) |
| CEERS-01244 | 215.24067 | 53.03606 | 4.478 | $42.89^{+0.01}_{-0.01}$ | $2228^{+75}_{-52}$ | $7.51^{+0.04}_{-0.03}$ | Harikane et al. (2023) |
| CEERS-01665 | 215.17821 | 53.05936 | 4.483 | $42.83^{+0.05}_{-0.04}$ | $1794^{+282}_{-171}$ | $7.28^{+0.15}_{-0.13}$ | Harikane et al. (2023) |
| CEERS-02782 | 214.82346 | 52.83028 | 5.241 | $42.88^{+0.04}_{-0.04}$ | $2534^{+260}_{-266}$ | $7.62^{+0.11}_{-0.12}$ | Harikane et al. (2023) |
| GOODS-N-13733 | 189.05708 | 62.26894 | 5.236 | $42.38^{+0.03}_{-0.04}$ | $2208^{+200}_{-200}$ | $7.49^{+0.10}_{-0.10}$ | Matthee et al. (2023) |
| GOODS-N-16813 | 189.17929 | 62.29253 | 5.355 | $42.65^{+0.05}_{-0.05}$ | $2033^{+219}_{-219}$ | $7.55^{+0.12}_{-0.12}$ | Matthee et al. (2023) |
| GOODS-N-4014 | 189.30013 | 62.21204 | 5.228 | $42.66^{+0.02}_{-0.02}$ | $2103^{+159}_{-159}$ | $7.58^{+0.08}_{-0.08}$ | Matthee et al. (2023) |
| GOODS-S-13971 | 53.13858 | -27.79025 | 5.481 | $42.40^{+0.08}_{-0.10}$ | $2192^{+479}_{-479}$ | $7.49^{+0.25}_{-0.25}$ | Matthee et al. (2023) |
| M23-10013704-2 | 53.12654 | -27.81809 | 5.919 | $41.99^{+0.03}_{-0.04}$ | $2416^{+179}_{-156}$ | $7.50^{+0.31}_{-0.31}$ | Maiolino et al. (2023) |
| M23-20621 | 189.12252 | 62.29285 | 4.681 | $42.00^{+0.03}_{-0.03}$ | $1638^{+148}_{-150}$ | $7.30^{+0.31}_{-0.31}$ | Maiolino et al. (2023) |
| M23-3608 | 189.11794 | 62.23552 | 5.269 | $41.46^{+0.10}_{-0.09}$ | $1373^{+361}_{-198}$ | $6.82^{+0.38}_{-0.33}$ | Maiolino et al. (2023) |
| M23-53757-2 | 189.26978 | 62.19421 | 4.448 | $42.03^{+0.04}_{-0.04}$ | $2416^{+179}_{-157}$ | $7.69^{+0.32}_{-0.31}$ | Maiolino et al. (2023) |
| M23-73488-2 | 189.19740 | 62.17723 | 4.133 | $42.52^{+0.01}_{-0.01}$ | $2160^{+45}_{-46}$ | $7.71^{+0.30}_{-0.30}$ | Maiolino et al. (2023) |
| M23-77652 | 189.29323 | 62.19900 | 5.229 | $42.09^{+0.02}_{-0.04}$ | $1070^{+219}_{-180}$ | $6.86^{+0.35}_{-0.34}$ | Maiolino et al. (2023) |
| M23-8083 | 53.13284 | -27.80186 | 4.648 | $41.92^{+0.02}_{-0.02}$ | $1648^{+127}_{-130}$ | $7.25^{+0.31}_{-0.31}$ | Maiolino et al. (2023) |

[1]The SMBH masses are calculated using the H$\alpha$ broad emission line. The errors in the table only contain statistical errors; the systematic errors of the black hole mass is about 0.3 dex.

clude observations where the target has an off-axis angle smaller than $8'$, and use circular apertures that correspond to an enclosed counts fraction (ECF) of 0.9. The background level is estimated using the square regions centered on the sources with sizes of $30'' \times 30''$, excluding the inner circular regions with a radius of $7''$. The background level is then subtracted from the stacked source flux. The output of CSTACK includes the stacked photon count rates and their errors in the soft $(0.5-2~\mathrm{keV})$ and hard $(2-8~\mathrm{keV})$ X-ray bands, as well as the stacked images of the sample.

To exclude objects that are not suitable for our stacking analysis (e.g., those with bright companions) and to enable a flexible analysis, we take the following steps to perform the stacking. We first run CSTACK for each individual object to stack all observations that cover this object. We then visually inspect the stacked images of individual objects and exclude those with bright companions or with uneven background, which can cause inaccurate background estimation and subtraction. We then run CSTACK again for the whole sample to get the stacked images.

Figure 1 presents the stacked images of our LRD sample, which do not show any signal at the central source position. The total exposure time of the stacked images is 26.0 Ms.

### 2.3. X-ray Flux Limits

We then evaluate the upper limit of the photon rate for individual LRDs and for the whole sample. Since our targets only have a few (or zero) photons in their source apertures, we need to use Poisson statistics instead of Gaussian distributions to describe the photon rates. We note that CSTACK estimates the error of the stacked flux by bootstrapping the sample, which does not work for individual objects. Here we derive the errors of the measured fluxes for individual objects using Poisson statistics.

Specifically, for the $i$th image to be stacked, CSTACK computes the photon rate of a source as follows:

$$r_{s,i} = \left[ \frac{N_i}{t_i} - \frac{N_{b,i} A_{s,i}}{t_{b,i} A_{b,i}} \right] / 0.9 \qquad (1)$$

where $N_i$ $(N_{b,i})$ is the number of photons within the source aperture (within the background region), $t_i$ $(t_{b,i})$
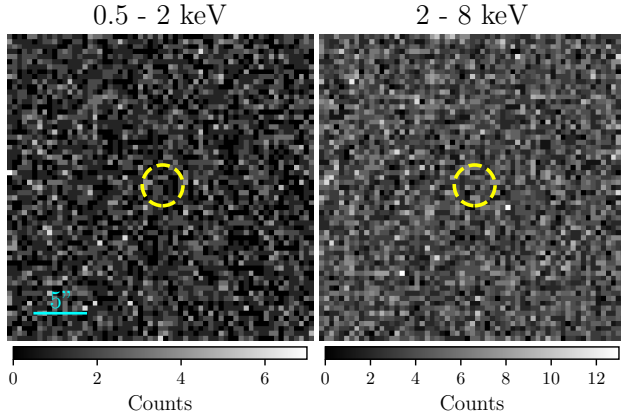
**Figure 1.** The stacked images (size $30'' \times 30''$) of LRDs in the soft (*left*) and hard (*right*) X-ray band produced by CSTACK. The total exposure time is 26.0 Ms. The yellow circles (with radii of $2''$) mark the source position. These images clearly show no X-ray detections of the LRD sample.

is the exposure time on the source (on the background region), and $A_{s,i}$ ($A_{b,i}$) is the area of the source aperture (background region). The factor 0.9 accounts for the ECF of the apertures.

CSTACK delivers the observed values of $N_i$ and $N_{b,i}$, which we denote as $N_i^{\text{obs}}$ and $N_{b,i}^{\text{obs}}$. These photon counts follow the Poisson distribution. In the following text, we use $N_i$ and $N_{b,i}$ to denote the expectation of the Poisson distributions. According to Bayes' Theorem, the probability for the observation to have an expected photon count of $N_i$ in the source aperture is

$$P(N_i|N_i^{\text{obs}}) = \frac{P(N_i^{\text{obs}}|N_i)P(N_i)}{P(N_i^{\text{obs}})} = \frac{N_i^{N_i^{\text{obs}}} e^{-N_i}}{N_i^{\text{obs}}!} \quad (2)$$

For the second equal sign, we assume a flat prior for $N_i$ and normalize the probabilistic distribution. Similarly, for $N_{b,i}$ we have

$$P(N_{b,i}|N_{b,i}^{\text{obs}}) = \frac{N_{b,i}^{N_{b,i}^{\text{obs}}} e^{-N_{b,i}}}{N_{b,i}^{\text{obs}}!} \quad (3)$$

The stacked photon rate, $r_s$, can then be computed by

$$r_s = \sum_i w_i r_{s,i} \quad (4)$$

where $w_i$ is the weight of the $i$th image in stacking. In this work, we use the exposure time as the weight of each image, i.e., $w_i \propto t_i$. The probabilistic distribution of $r_s$ can be determined by combining Equation 1, 2, 3, and 4.

Table 2 lists the evaluated fluxes and errors for individual LRDs, as well as for the whole sample. None

of the LRDs are detected individually in either the soft or the hard band, and stacking the whole sample also results in non-detections in the two bands. In the rest of this Letter, we define upper limits as the values corresponding to a cumulative probability of 99.87%. This definition is equivalent to a $3\sigma$ upper limit in a Gaussian distribution.

### 2.4. *Estimating Physical Fluxes and Luminosities*

As the next step, we convert photon rates to physical fluxes. Following the manual of CSTACK, we convert photon rates (in counts s$^{-1}$) to fluxes (in erg s$^{-1}$cm$^{-2}$) using the *Chandra* Proposal Planning Toolkit[3]. We use a power law with photon index $\Gamma = 1.8$ to describe the unabsorbed X-ray spectra of LRDs, and assume $N_H = 10^{22}$ cm$^{-2}$ for the AGN photoelectric absorption. These values are found typical for type-I AGNs (e.g., Koss et al. 2017; Ricci et al. 2017; Panagiotou & Walter 2019). For the Milky Way absorption, we assume $N_{\text{H}} = 10^{20}$ cm$^{-2}$, which is determined using the online HEASoft tool[4], where we adopt the column density map from HI4PI Collaboration et al. (2016). We also compute the upper limits of the unabsorbed X-ray luminosities at rest-frame 2 to 10 keV ($L_{\text{X}}$) for the LRDs. We find that the soft band gives tighter constraints on $L_{\text{X}}$ compared to the hard band, so we use soft band fluxes to compute the upper limits of $L_{\text{X}}$. The results of this conversion are listed in Table 2.

All the data and code used in this work will be made publicly available upon publication of this Letter.

### 3. RESULTS

We now consider the implication of the X-ray non-detections. The key argument in support of the hypothesis that AGN are present in LRDs is the observation of broad Balmer, e.g., H$\alpha$, emission lines. However, type-I AGN activity is not the only plausible source of broad H$\alpha$ lines. Outflows driven by star formation (e.g., Arribas et al. 2014; Davies et al. 2019; Förster Schreiber & Wuyts 2020) and supernovae (e.g., Baldassare et al. 2016) can also produce broad H$\alpha$ emission lines. To test whether the broad H$\alpha$ lines are indeed linked to AGN activity, we consider the relation between the X-ray luminosity and the H$\alpha$ luminosity that has been found in low-redshift AGNs (e.g., Ho et al. 2001; Shi et al. 2010). Specifically, we adopt the relation measured by Jin et al.

[3] https://cxc.harvard.edu/toolkit/pimms.jsp

[4] https://heasarc.gsfc.nasa.gov/cgi-bin/Tools/w3nh/w3nh.pl

**Table 2.** Stacking results for individual objects and the whole sample

| Name | Rate$_\mathrm{soft}$ | Rate$_\mathrm{hard}$ | $F_\mathrm{soft}$ | $F_\mathrm{hard}$ | $L_\mathrm{X}$ (from soft) | $L_\mathrm{X}$ (from hard) |
|---|---|---|---|---|---|---|
| | $(10^{-6}\mathrm{cts\ s^{-1}})$ | $(10^{-6}\mathrm{cts\ s^{-1}})$ | $(10^{-17}\mathrm{erg\ s^{-1}cm^{-2}})$ | $(10^{-17}\mathrm{erg\ s^{-1}cm^{-2}})$ | $(10^{43}\mathrm{erg\ s^{-1}})$ | $(10^{43}\mathrm{erg\ s^{-1}})$ |
| CEERS-00397 | $1.45^{+4.72}_{-3.90}$ | $-2.29^{+7.83}_{-6.20}$ | $0.82^{+2.66}_{-2.20}$ | $-3.87^{+13.21}_{-10.46}$ | $< 4.92$ | $< 14.33$ |
| CEERS-00672 | $-1.56^{+2.14}_{-0.74}$ | $1.90^{+5.55}_{-4.84}$ | $-0.88^{+1.21}_{-0.42}$ | $3.21^{+9.37}_{-8.17}$ | $< 1.87$ | $< 12.02$ |
| CEERS-00717 | $-0.66^{+2.17}_{-0.89}$ | $2.14^{+4.83}_{-4.10}$ | $-0.37^{+1.23}_{-0.50}$ | $3.62^{+8.15}_{-6.91}$ | $< 3.40$ | $< 17.37$ |
| CEERS-00746 | $-0.61^{+2.95}_{-1.69}$ | $5.84^{+6.30}_{-6.45}$ | $-0.34^{+1.66}_{-0.95}$ | $9.87^{+10.64}_{-10.89}$ | $< 2.62$ | $< 15.68$ |
| CEERS-01236 | $1.62^{+3.77}_{-3.00}$ | $2.01^{+6.48}_{-5.79}$ | $0.91^{+2.11}_{-1.68}$ | $3.40^{+10.93}_{-9.77}$ | $< 2.29$ | $< 8.12$ |
| CEERS-01244 | $-7.35^{+7.79}_{-5.16}$ | $9.76^{+13.61}_{-14.77}$ | $-4.12^{+4.36}_{-2.89}$ | $16.47^{+22.98}_{-24.94}$ | $< 2.26$ | $< 17.84$ |
| CEERS-01665 | $12.26^{+5.61}_{-7.25}$ | $-10.88^{+10.23}_{-6.89}$ | $6.87^{+3.14}_{-4.06}$ | $-18.36^{+17.27}_{-11.63}$ | $< 4.84$ | $< 6.14$ |
| CEERS-02782 | $1.99^{+2.55}_{-1.88}$ | $-1.17^{+3.52}_{-2.14}$ | $1.12^{+1.43}_{-1.06}$ | $-1.98^{+5.94}_{-3.62}$ | $< 2.64$ | $< 5.74$ |
| GOODS-N-13733 | $0.14^{+3.20}_{-2.78}$ | $5.42^{+5.14}_{-5.88}$ | $0.06^{+1.46}_{-1.27}$ | $10.07^{+9.55}_{-10.94}$ | $< 1.69$ | $< 11.67$ |
| GOODS-N-16813 | $-1.97^{+2.55}_{-1.48}$ | $9.23^{+4.98}_{-6.36}$ | $-0.90^{+1.16}_{-0.67}$ | $17.15^{+9.25}_{-11.82}$ | $< 1.15$ | $< 14.93$ |
| GOODS-N-4014 | $1.51^{+2.24}_{-2.08}$ | $0.54^{+3.85}_{-3.48}$ | $0.69^{+1.02}_{-0.95}$ | $1.00^{+7.16}_{-6.47}$ | $< 1.54$ | $< 6.70$ |
| GOODS-S-13971 | $-0.19^{+0.59}_{-0.32}$ | $-1.56^{+1.45}_{-0.86}$ | $-0.11^{+0.35}_{-0.19}$ | $-2.73^{+2.54}_{-1.51}$ | $< 0.49$ | $< 1.56$ |
| M23-10013704-2 | $-0.48^{+0.50}_{-0.15}$ | $-0.29^{+1.47}_{-1.13}$ | $-0.28^{+0.29}_{-0.09}$ | $-0.51^{+2.57}_{-1.98}$ | $< 0.46$ | $< 2.94$ |
| M23-20621 | $-3.42^{+2.30}_{-1.05}$ | $3.80^{+4.95}_{-5.27}$ | $-1.56^{+1.05}_{-0.48}$ | $7.07^{+9.20}_{-9.80}$ | $< 0.49$ | $< 8.19$ |
| M23-3608 | $2.92^{+2.59}_{-2.48}$ | $2.41^{+4.20}_{-3.97}$ | $1.33^{+1.18}_{-1.13}$ | $4.48^{+7.80}_{-7.38}$ | $< 2.15$ | $< 9.01$ |
| M23-53757-2 | $5.74^{+2.49}_{-3.22}$ | $9.80^{+3.94}_{-5.58}$ | $2.61^{+1.13}_{-1.47}$ | $18.22^{+7.32}_{-10.37}$ | $< 1.77$ | $< 8.99$ |
| M23-73488-2 | $1.80^{+2.02}_{-1.89}$ | $2.64^{+3.53}_{-3.59}$ | $0.82^{+0.92}_{-0.86}$ | $4.91^{+6.57}_{-6.68}$ | $< 0.92$ | $< 4.56$ |
| M23-77652 | $0.08^{+2.15}_{-1.70}$ | $-0.73^{+3.97}_{-3.35}$ | $0.04^{+0.98}_{-0.77}$ | $-1.36^{+7.38}_{-6.22}$ | $< 1.21$ | $< 6.03$ |
| M23-8083 | $0.35^{+0.83}_{-0.62}$ | $0.40^{+1.63}_{-1.41}$ | $0.21^{+0.48}_{-0.36}$ | $0.75^{+3.02}_{-2.62}$ | $< 0.59$ | $< 2.40$ |
| Sample Stack | $0.30^{+0.74}_{-0.68}$ | $3.11^{+1.47}_{-1.41}$ | $-$ | $-$ | $-$ | $-$ |

NOTE—For the rates and fluxes, the values are the 16th, 50th, and 84th percentiles of the distributions. The Upper limits of luminosities correspond to a cumulative probability of 0.9987, which is equivalent to $3\sigma$ limits of Gaussian distributions.

(2012a), i.e.,

$$\log L_\mathrm{X}[\mathrm{erg\ s^{-1}}] = 0.83 \times \log L_{\mathrm{H}\alpha}[\mathrm{erg\ s^{-1}}] + 8.35 \quad (5)$$
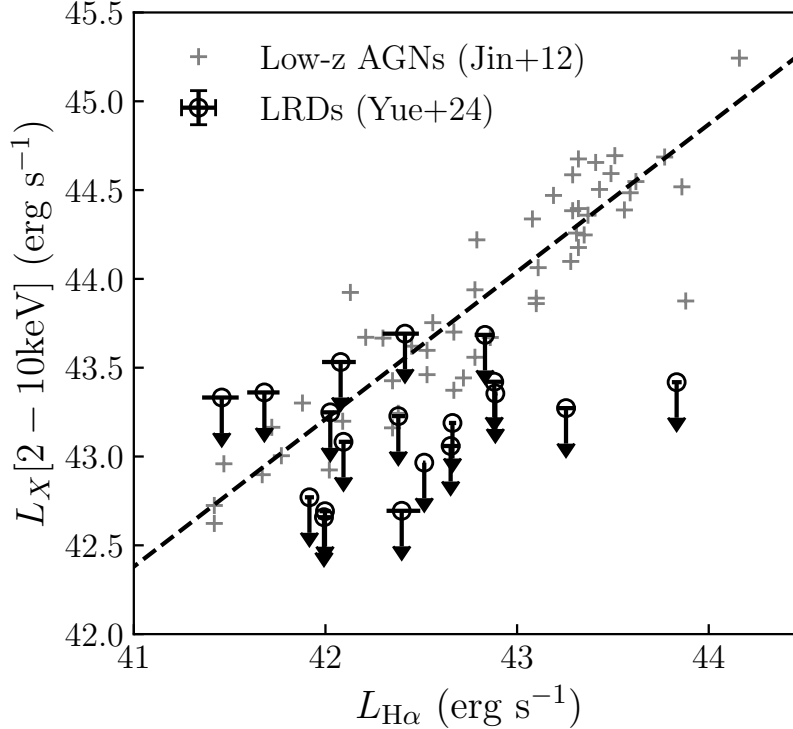
The scatter of this relation is about 0.3 dex. Note that the H$\alpha$ luminosity in this relation corresponds to the broad H$\alpha$ component. Assuming that the X-ray emissions and the broad H$\alpha$ lines of LRDs are produced in the same way as the emission in low-redshift type-I AGNs, we expect that these objects should follow the observed $L_\mathrm{X} - L_{\mathrm{H}\alpha}$ relation[5].

Figure 2 shows the $L_\mathrm{X} - L_{\mathrm{H}\alpha}$ relation for low-redshift AGNs and for the LRDs. Most LRDs lie below the $L_\mathrm{X} - L_{\mathrm{H}\alpha}$ relation. In particular, several LRDs with $L_{\mathrm{H}\alpha} \gtrsim 10^{43}$ erg s$^{-1}$ have X-ray upper limits that are

[5] We notice that $L_\mathrm{X}$ also tightly correlates with optical and [O III] luminosities (e.g., Heckman et al. 2005; Lusso et al. 2010). Nevertheless, most LRDs in our sample do not have [O III] emission line measurements, and the contribution of the host galaxy to the optical continuum and [O III] luminosity is highly uncertain. In contrast, all LRDs in our sample have spectroscopically-confirmed broad H$\alpha$ lines, and thus we focus on the $L_\mathrm{X} - L_{\mathrm{H}\alpha}$ relation.

$\sim 1-2$ dex weaker than expected from the $L_\mathrm{X} - L_{\mathrm{H}\alpha}$ relation. This result indicates that, at least for LRDs with the strongest H$\alpha$ emissions, the X-ray emission is exceptionally weak. A recent study by Wang et al. (2024) also found similar results, who investigated a luminous LRD at $z = 3.1$ and concluded that its X-ray emission must be about 100 times fainter than the expected value given its optical luminosity.

Stacking the whole sample allows us to put a more stringent constraint on the X-ray fluxes of the entire LRD population. Since the LRDs have different redshifts, it is not clear how to convert the stacked photon counts to physical fluxes and rest-frame luminosities. Instead, we convert the H$\alpha$ luminosities to the expected photon rates for individual LRDs, and average these expected rates using the same weight when stacking (i.e., the exposure time, see Eqn. 4) to evaluate the expected stacked photon rates. The results are shown in Figure 3. In the soft band, the upper limit of the stacked rate is $\sim 1$ dex lower than the expected value derived from the H$\alpha$ luminosity. This result indicates again that the soft X-ray emissions of LRDs are significantly weaker than

**Figure 2.** The $L_{\mathrm{X}} - L_{\mathrm{H}\alpha}$ relation. The gray crosses represent low-redshift type-I AGNs from Jin et al. (2012c). The dashed line marks the relation as given by Equation 5. The open circles are the upper limits derived using the soft-band flux limits for individual LRDs. Most of the upper limits are below the $L_{\mathrm{X}} - L_{\mathrm{H}\alpha}$ relation; in particular, the two LRDs with the largest H$\alpha$ luminosities have X-ray upper limits $\sim 1 - 2$ dex lower than the relation.

typical type-I AGNs. However, the stacked photon rate in the hard band is still consistent with the expected level.

## 4. DISCUSSION

The X-ray non-detections of LRDs, even after stacking, indicate that there are some key differences between LRDs and low-redshift type-I AGNs. In this Section, we discuss possible explanations to the X-ray non-detections for LRDs.

### 4.1. *Strong X-ray Absorption*

We first consider the possibility that the faint X-ray emission is a result of absorption. In our model, we assume a hydrogen column density of $N_{\mathrm{H}} = 10^{22}$ cm$^{-2}$ for LRDs, which is typical for type-I AGNs. To test how this assumption influences our result, we change the column density to $10^{23}$ cm$^{-2}$ for the AGN component, which gives an expected soft-band count rate that is 0.9 dex higher than the observed value. To move the stacked count rate to the mean $L_{\mathrm{X}} - L_{\mathrm{H}\alpha}$ relation, we need to adopt a column density of $10^{24.2}$ cm$^{-2}$, putting these AGNs into the Compton thick regime. We also note that $N_H$ has little impact on the expected hard band count rate.

Most type-I AGNs have $N_{\mathrm{H}} \sim 10^{20} - 10^{23}$ cm$^{-2}$ (e.g., Koss et al. 2017; Panagiotou & Walter 2019; Ananna et al. 2022a). Since the LRDs in our sample exhibit broad H$\alpha$ lines, it is highly unlikely that these objects have such high column densities of $\gtrsim 10^{24}$ cm$^{-2}$. Some broad absorption line (BAL) quasars have high column densities ($N_{\mathrm{H}} \gtrsim 10^{24}$ cm$^{-2}$; e.g., Blustin et al. 2008; Rogerson et al. 2011), though LRDs with rest-frame UV spectra do not show strong BAL features (e.g., Greene et al. 2023; Maiolino et al. 2023). We also notice that some low-redshift type-I AGNs have $N_{\mathrm{H}} > 10^{24}$cm$^{-2}$ (e.g., Ananna et al. 2022b); however, these AGNs are very rare, which only occupy a small fraction ($\lesssim 5\%$) of the entire type-I AGN population. In comparison, LRDs are numerous, the number density of which is $\sim 1$ dex higher than the quasar luminosity function and is only $\sim 2$ dex lower than the galaxy luminosity function at similar redshifts (Greene et al. 2023; Kocevski et al. 2024). We thus consider it unlikely that absorption is the only reason for the low X-ray fluxes of LRDs.

### 4.2. *Intrinsically faint X-ray emission*

Alternatively, we suggest that LRDs might be a population of AGNs with intrinsically-faint X-ray emission, implying a low $L_{\mathrm{X}}/L_{\mathrm{H}\alpha}$ ratio. Specifically, the inner ac-
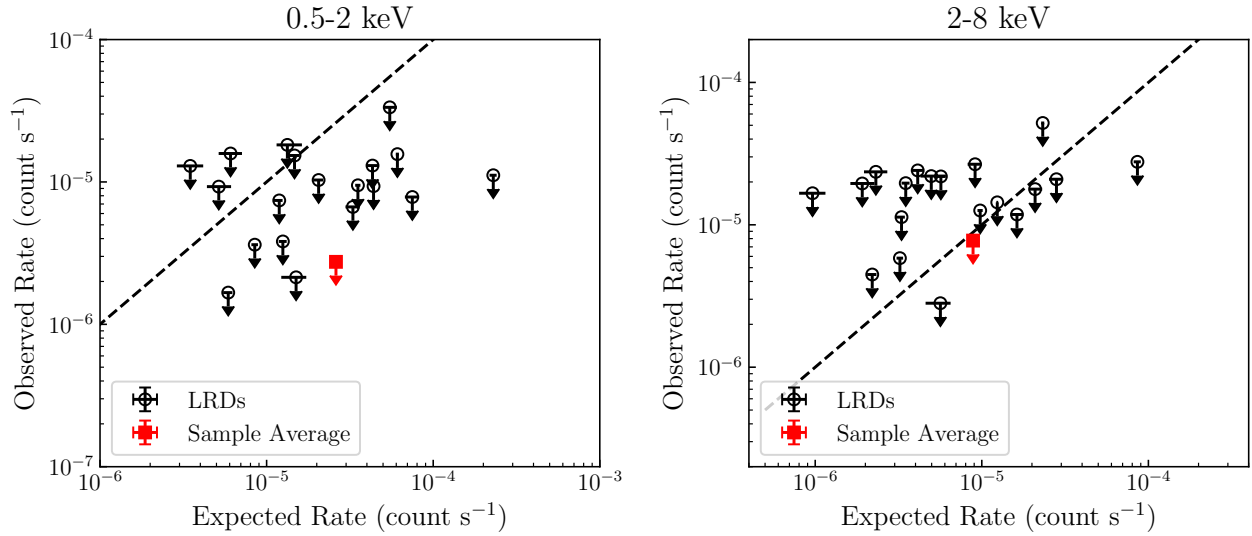
**Figure 3.** *Left:* comparing the soft band stacked rate (the red square) with the expected value from the Hα luminosities. The dashed line marks the $x = y$ relation in this plot. The upper limit of the stacked rate is $\sim 1$ dex below the expected flux. *Right:* same as the left panel, but for the hard band. The stacked flux in the hard band is consistent with the expected value.

cretion disk and the corona of LRDs might be different from other type-I AGNs. It is also possible that LRDs have unique broad line region properties, such that their Hα line fluxes are higher than other type-I AGNs.

Previous studies have pointed out that the ratio between optical and X-ray fluxes for AGNs (i.e., $\alpha_{\rm OX}$) increases with Eddington ratio (e.g., Vasudevan & Fabian 2007; Jin et al. 2012b). The Eddington ratios of LRDs have been estimated to be $\lambda_{\rm Edd} \sim 0.05-2$ (e.g., Harikane et al. 2023; Maiolino et al. 2023), which is comparable to the AGN sample used to derive the $L_{\rm X}-L_{\rm H\alpha}$ relation in Jin et al. (2012a). However, we note that the intrinsic Eddington ratio of LRDs might be higher than the reported values due to dust attenuation (e.g., Matthee et al. 2023). Therefore, high Eddington ratios might contribute to the low observed $L_{\rm X}/L_{\rm H\alpha}$ ratios of LRDs. Since the estimated Eddington ratios of LRDs, however, still have large uncertainties, we leave a more quantitative investigation to future studies.

We note that the intrinsic $L_{\rm X}/L_{\rm H\alpha}$ ratios of LRDs might be even lower than indicated in Figure 2. Most current modes of LRDs suggest large dust attenuations ($A_V \gtrsim 2$; e.g., Pérez-González et al. 2024; Kocevski et al. 2024). Furthermore, some models have suggested that the broad emission lines of LRDs are produced by scattered light from the central type-I AGN, which is only a small fraction of the intrinsic emissions (e.g., Greene et al. 2023). Consequently, the intrinsic Hα luminosities of LRDs might be larger than the observed values, leading to lower intrinsic $L_{\rm X}/L_{\rm H\alpha}$ ratios.

### 4.3. Broad Balmer emission lines due to outflows

Another plausible scenario is that AGN activity has little or no contribution to the observed broad Hα lines of LRDs. Some other mechanisms have also been proposed that can produce Hα emission lines with FWHM$\gtrsim$ 1000 km s$^{-1}$, including strong outflows driven by star formation or supernovae (e.g., Baldassare et al. 2016; Davies et al. 2019; Förster Schreiber & Wuyts 2020). This hypothesis agrees with the result from recent MIRI observations (Pérez-González et al. 2024), which found that starburst galaxies might have a major contribution to the near-to-mid infrared SED of LRDs. Future *JWST*/NIRSpec observations will characterize the fluxes, kinematics, and spatial extents of the UV and optical emission lines, which will provide more clues about the contribution of outflows to the broad Hα lines.

In any case, our results indicate that we need to be cautious when applying previous knowledge about type-I AGNs to these LRDs. In particular, the bolometric luminosities and the SMBH masses of LRDs estimated from the scaling relations for type-I AGNs might have significant systematic uncertainties.

### 5. CONCLUSIONS

We investigate the X-ray properties of 19 LRDs using a stacking analysis. The LRD sample is compiled from the literature and is selected to show broad Hα emission lines with FWHM > 1000 km s$^{-1}$, indicating possible type-I AGN activity. After stacking archival *Chandra* data, we do not detect the X-ray emission of the LRDs, and put stringent upper limits on their X-ray fluxes. The upper limit on the soft-band flux is $\sim 1$ dex lower than the expected level from the $L_{\rm X}-L_{\rm H\alpha}$ relation of

low-redshift type-I AGN, while the upper limit on the hard band flux is consistent with the relation.

Our result suggests that LRDs might have different properties compared to the typical type-I AGN population. Specifically, we consider it unlikely that the observed low X-ray fluxes of LRDs are purely resulted from absorption. Alternatively, we discuss two plausible hypotheses to explain the observed low $L_{\rm X}/L_{\rm H\alpha}$ ratios: (1) LRDs have intrinsically weak X-ray emissions; (2) outflows have a major contribution to the observed broad $H\alpha$ emission lines. In any case, caution should be taken when applying the empirical relations derived from other type-I AGNs to the LRD population.

The sample of LRDs is rapidly increasing thanks to the ongoing imaging and spectroscopic surveys with *JWST*. With a larger LRD sample in the near future, we expect that a stacking analysis will put even stronger constraints on the X-ray properties of LRDs. Further-

more, upcoming *JWST*/NIRSpec observations will reveal the fluxes, kinematics, and spatial extents of the other optical and UV emission lines of LRDs, shedding more light on the nature of this population. Future X-ray missions, such as the Advanced X-Ray Imaging Satellite (AXIS; Reynolds et al. 2023), will offer much deeper images than *Chandra* and will likely solve the puzzles about the X-ray properties of LRDs.

*Facilities:* Chandra(ACIS-I)

*Software:* cstack, stackfast, sherpa, xspec

## REFERENCES

Ananna, T. T., Weigel, A. K., Trakhtenbrot, B., et al. 2022a, ApJS, 261, 9, doi: 10.3847/1538-4365/ac5b64

Ananna, T. T., Urry, C. M., Ricci, C., et al. 2022b, ApJL, 939, L13, doi: 10.3847/2041-8213/ac9979

Arribas, S., Colina, L., Bellocchi, E., Maiolino, R., & Villar-Martín, M. 2014, A&A, 568, A14, doi: 10.1051/0004-6361/201323324

Baldassare, V. F., Reines, A. E., Gallo, E., et al. 2016, ApJ, 829, 57, doi: 10.3847/0004-637X/829/1/57

Blustin, A. J., Dwelly, T., Page, M. J., et al. 2008, MNRAS, 390, 1229, doi: 10.1111/j.1365-2966.2008.13825.x

Brandt, W. N., Hornschemeier, A. E., Alexander, D. M., et al. 2001, AJ, 122, 1, doi: 10.1086/321135

Davies, R. L., Förster Schreiber, N. M., Übler, H., et al. 2019, ApJ, 873, 122, doi: 10.3847/1538-4357/ab06f1

Förster Schreiber, N. M., & Wuyts, S. 2020, ARA&A, 58, 661, doi: 10.1146/annurev-astro-032620-021910

Greene, J. E., Labbe, I., Goulding, A. D., et al. 2023, arXiv e-prints, arXiv:2309.05714, doi: 10.48550/arXiv.2309.05714

Harikane, Y., Zhang, Y., Nakajima, K., et al. 2023, ApJ, 959, 39, doi: 10.3847/1538-4357/ad029e

Heckman, T. M., Ptak, A., Hornschemeier, A., & Kauffmann, G. 2005, ApJ, 634, 161, doi: 10.1086/491665

HI4PI Collaboration, Ben Bekhti, N., Flöer, L., et al. 2016, A&A, 594, A116, doi: 10.1051/0004-6361/201629178

Ho, L. C., Feigelson, E. D., Townsley, L. K., et al. 2001, ApJL, 549, L51, doi: 10.1086/319138

Inayoshi, K., & Ichikawa, K. 2024, arXiv e-prints, arXiv:2402.14706, doi: 10.48550/arXiv.2402.14706

Jin, C., Ward, M., & Done, C. 2012a, MNRAS, 422, 3268, doi: 10.1111/j.1365-2966.2012.20847.x

—. 2012b, MNRAS, 425, 907, doi: 10.1111/j.1365-2966.2012.21272.x

Jin, C., Ward, M., Done, C., & Gelbord, J. 2012c, MNRAS, 420, 1825, doi: 10.1111/j.1365-2966.2011.19805.x

Kocevski, D. D., Onoue, M., Inayoshi, K., et al. 2023, ApJL, 954, L4, doi: 10.3847/2041-8213/ace5a0

Kocevski, D. D., Finkelstein, S. L., Barro, G., et al. 2024, arXiv e-prints, arXiv:2404.03576, doi: 10.48550/arXiv.2404.03576

Koss, M., Trakhtenbrot, B., Ricci, C., et al. 2017, ApJ, 850, 74, doi: 10.3847/1538-4357/aa8ec9

Labbe, I., Greene, J. E., Bezanson, R., et al. 2023, arXiv e-prints, arXiv:2306.07320, doi: 10.48550/arXiv.2306.07320

Laird, E. S., Nandra, K., Georgakakis, A., et al. 2009, ApJS, 180, 102, doi: 10.1088/0067-0049/180/1/102

Lusso, E., Comastri, A., Vignali, C., et al. 2010, A&A, 512, A34, doi: 10.1051/0004-6361/200913298

Lyu, J., Alberts, S., Rieke, G. H., et al. 2023, arXiv e-prints, arXiv:2310.12330, doi: 10.48550/arXiv.2310.12330

Maiolino, R., Scholtz, J., Curtis-Lake, E., et al. 2023, arXiv e-prints, arXiv:2308.01230, doi: 10.48550/arXiv.2308.01230

Matsuoka, Y., Strauss, M. A., Kashikawa, N., et al. 2018, ApJ, 869, 150, doi: 10.3847/1538-4357/aaee7a

Matthee, J., Naidu, R. P., Brammer, G., et al. 2023, arXiv e-prints, arXiv:2306.05448, doi: 10.48550/arXiv.2306.05448

Miyaji, T., Griffiths, R. E., & C-COSMOS Team. 2008, in AAS/High Energy Astrophysics Division, Vol. 10, AAS/High Energy Astrophysics Division #10, 4.01

Noboriguchi, A., Inoue, A. K., Nagao, T., Toba, Y., & Misawa, T. 2023, ApJL, 959, L14, doi: 10.3847/2041-8213/ad0e00

Panagiotou, C., & Walter, R. 2019, A&A, 626, A40, doi: 10.1051/0004-6361/201935052

Pérez-González, P. G., Barro, G., Rieke, G. H., et al. 2024, arXiv e-prints, arXiv:2401.08782, doi: 10.48550/arXiv.2401.08782

Reynolds, C. S., Kara, E. A., Mushotzky, R. F., et al. 2023, in Society of Photo-Optical Instrumentation Engineers (SPIE) Conference Series, Vol. 12678, UV, X-Ray, and Gamma-Ray Space Instrumentation for Astronomy XXIII, ed. O. H. Siegmund & K. Hoadley, 126781E, doi: 10.1117/12.2677468

Ricci, C., Trakhtenbrot, B., Koss, M. J., et al. 2017, ApJS, 233, 17, doi: 10.3847/1538-4365/aa96ad

Rogerson, J. A., Hall, P. B., Snedden, S. A., Brotherton, M. S., & Anderson, S. F. 2011, NewA, 16, 128, doi: 10.1016/j.newast.2010.07.002

Rosati, P., Tozzi, P., Giacconi, R., et al. 2002, ApJ, 566, 667, doi: 10.1086/338339

Schindler, J.-T., Bañados, E., Connor, T., et al. 2023, ApJ, 943, 67, doi: 10.3847/1538-4357/aca7ca

Shi, Y., Rieke, G. H., Smith, P., et al. 2010, ApJ, 714, 115, doi: 10.1088/0004-637X/714/1/115

Vasudevan, R. V., & Fabian, A. C. 2007, MNRAS, 381, 1235, doi: 10.1111/j.1365-2966.2007.12328.x

Wang, B., de Graaff, A., Davies, R. L., et al. 2024, arXiv e-prints, arXiv:2403.02304, doi: 10.48550/arXiv.2403.02304